The Astrophysical Journal Letters, 884:L52 (7pp), 2019 October 20 https://doi.org/10.3847/2041-8213/ab4ae4

Nearly all Massive Quiescent Disk Galaxies Have a Surprisingly Large Atomic Gas Reservoir

Chengpeng Zhang[1,2], Yingjie Peng[1], Luis C. Ho[1,2], Roberto Maiolino[3,4], Avishai Dekel[5,6], Qi Guo[7,8], Filippo Mannucci[9], Di Li[8,10], Feng Yuan[11], Alvio Renzini[12], Jing Dou[1,2], Kexin Guo[1,13], Zhongyi Man[1,2], and Qiong Li[1,2]

[1] Kavli Institute for Astronomy and Astrophysics, Peking University, 5 Yiheyuan Road, Beijing 100871, People's Republic of China; yjpeng@pku.edu.cn
[2] Department of Astronomy, School of Physics, Peking University, 5 Yiheyuan Road, Beijing 100871, People's Republic of China
[3] Cavendish Laboratory, University of Cambridge, 19 J.J. Thomson Avenue, Cambridge CB3 0HE, UK
[4] Kavli Institute for Cosmology, University of Cambridge, Madingley Road, Cambridge CB3 0HA, UK
[5] Racah Institute of Physics, The Hebrew University, Jerusalem 91904, Israel
[6] SCIPP, University of California, Santa Cruz, CA 95064, USA
[7] Key Laboratory for Computational Astrophysics, National Astronomical Observatories, Chinese Academy of Sciences, Beijing 100012, People's Republic of China
[8] School of Astronomy and Space Science, University of Chinese Academy of Sciences, Beijing 100049, People's Republic of China
[9] Istituto Nazionale di Astrofisica, Osservatorio Astrofisico di Arcetri, Largo Enrico Fermi 5, I-50125 Firenze, Italy
[10] CAS Key Laboratory of FAST, National Astronomical Observatories, Chinese Academy of Sciences, Beijing 100012, People's Republic of China
[11] Key Laboratory for Research in Galaxies and Cosmology, Shanghai Astronomical Observatory, Chinese Academy of Sciences, 80 Nandan Road, Shanghai 200030, People's Republic of China
[12] INAF—Osservatorio Astronomico di Padova, Vicolo dell'Osservatorio 5, I-35122 Padova, Italy
[13] International Centre for Radio Astronomy Research, University of Western Australia, Crawley, WA 6009, Australia
Received 2019 August 1; revised 2019 September 9; accepted 2019 October 3; published 2019 October 18

Abstract

The massive galaxy population above the characteristic Schechter mass $M_* \approx 10^{10.6}\,M_\odot$ contributes to about half of the total stellar mass in the local universe. These massive galaxies usually reside in hot dark matter halos above the critical shock-heating mass $\sim 10^{12}\,M_\odot$, where the external cold gas supply to these galaxies is expected to be suppressed. When galaxies run out of their cold gas reservoir, they become dead and quiescent. Therefore, massive quiescent galaxies living in hot halos are commonly believed to be gas-poor. Based on the data from SDSS, ALFALFA, GASS, and COLD GASS surveys, here we show that the vast majority of the massive, quiescent, central disk galaxies in the nearby universe have a remarkably large amount of cold atomic hydrogen gas, surprisingly similar to star-forming galaxies. Both star-forming and quiescent disk galaxies show identical symmetric double-horn H I spectra, indicating similar regularly rotating H I disks. Relative to their star-forming counterparts, massive quiescent central disk galaxies are quenched because of their significantly reduced molecular gas content, lower dust content, and lower star formation efficiency. Our findings reveal a new picture, which clearly demonstrates the detailed star formation quenching process in massive galaxies and provides a stringent constraint on the physical mechanism of quenching.

Unified Astronomy Thesaurus concepts: Galaxy evolution (594); Interstellar medium (847); Galaxy quenching (2040); Interstellar atomic gas (833)

1. Introduction

Identifying the physical mechanism responsible for star formation quenching is one of the most debated open questions. In general, the level of star formation in the galaxy is controlled by its cold gas reservoir and star formation efficiency. Investigating the cold gas content in galaxies will provide direct observational evidence of how quenching may happen.

On average, the cold gas reservoir of quiescent galaxies was found to be significantly less than that of star-forming galaxies (e.g., Fabello et al. 2011; Huang et al. 2012; Brown et al. 2015; Saintonge et al. 2016; Catinella et al. 2018; Tacconi et al. 2018). However, some quiescent galaxies were found to have a large amount of H I gas content (e.g., Schommer & Bothun 1983; Geréb et al. 2016, 2018; George et al. 2019; Parkash et al. 2019). On the other hand, although the majority of quiescent galaxies are ellipticals or lenticulars (Emsellem et al. 2011), there exists a significant population of red spiral galaxies (e.g., Masters et al. 2010; Tojeiro et al. 2013). Various physical mechanisms for quenching star formation are currently entertained, such as AGN feedback (Croton et al. 2006; Fabian 2012; Harrison 2017), environmental effects (Kauffmann et al. 2004; Baldry et al. 2006; Peng et al. 2012), major merger (Mihos & Hernquist 1996; Hopkins et al. 2008), halo quenching (Dekel & Birnboim 2006), morphological quenching (Martig et al. 2009), gravitational quenching (Genzel et al. 2014), and strangulation (Larson et al. 1980; Peng et al. 2015). The morphological differences among quenched galaxies may be related to the specific mechanism that was responsible for their quenching.

Investigating the cold gas content in different quiescent galaxies, such as, central/satellite, disk/elliptical galaxies, may provide stringent constraints on different quenching mechanisms. In this study, we focus on the cold gas content in central galaxies above the characteristic Schechter mass $M_* \approx 10^{10.6}\,M_\odot$. These massive galaxies usually reside in hot dark matter halos above the critical shock-heating mass $M_{\rm shock} \approx 10^{12}\,M_\odot$ (Dekel & Birnboim 2006), where the external cold gas supply to these galaxies is expected to be suppressed (Dekel & Birnboim 2006, 2008). Using the data from multiwavelength sky surveys, here we show that the vast majority of the massive quiescent central galaxies with disk morphologies still have a large amount of cold atomic hydrogen gas, surprisingly similar to star-forming galaxies. We further show that the reason of the low-level star formation in these galaxies is the significantly

lower molecular gas mass and lower star formation efficiency of the molecular gas. The Chabrier (2003) initial mass function (IMF) is used throughout this work and we assume the following cosmological parameters: $\Omega_m = 0.3$, $\Omega_\Lambda = 0.7$, $H_0 = 70\ \mathrm{km\ s^{-1}\ Mpc^{-1}}$.

2. Sample

2.1. Sloan Digital Sky Survey (SDSS)

The parent galaxy sample analyzed in this paper is the same SDSS (Abazajian et al. 2009) DR7 sample that we constructed in Peng et al. (2010, 2012, 2015). The parent photometric sample contains 1,579,314 objects after removing duplicates, of which 72,697 have reliable spectroscopic redshift measurements in the redshift range $0.02 < z < 0.05$.

The stellar masses (M_*) for the SDSS galaxies are determined from the *k*-correction program v4_1_4 (Blanton & Roweis 2007) with stellar population synthesis models of Bruzual & Charlot (2003). The derived stellar masses are highly consistent with the published stellar masses of Kauffmann et al. (2003) with a small difference of ∼0.1 dex. The star formation rates (SFRs) are taken from the value-added MPA-JHU SDSS DR7 catalog (Brinchmann et al. 2004) and converted to Chabrier IMF. These SFRs are based on Hα emission-line luminosities, corrected for extinction using the Hα/Hβ ratio. To correct for the aperture effects, the SFRs outside the SDSS 3″ fiber were obtained by performing the spectral energy distribution (SED) fitting to the *ugriz* photometry outside the fiber, using the models and methods described in Salim et al. (2007). Since the Hα emission of AGN and composite galaxies are likely to be contaminated by their nuclear activity, their SFRs are derived based on the strength of the 4000 Å break as calibrated with Hα for non-AGN, pure star-forming galaxies (see details in Brinchmann et al. 2004).

We classify our sample into central galaxies and satellite galaxies using the SDSS DR7 group catalog from Yang et al. (2005, 2007). To reduce the contamination of the central sample by spurious interlopers into the group, we define central galaxies to be simultaneously both the most massive and the most luminous (in *r*-band) galaxy within a given group. The centrals also include single galaxies that do not have identified companions above the SDSS flux limit.

The morphology classifications are from the Galaxy Zoo (GZ) project (Lintott et al. 2011). In GZ, the image of each galaxy was viewed and classified by dozens of volunteers and a morphology flag ("spiral," "elliptical," or "uncertain") is assigned to each galaxy after a debiasing process. Most lenticular/S0 galaxies with smooth and rounded profiles are classified in GZ as "elliptical" or "uncertain." Since "spirals" in GZ include disk galaxies with or without clear spiral arms, we simply designate all galaxies classified as "spiral" in GZ as "disk" galaxies. In total, 3% of these galaxies are excluded because their P_MG values in GZ are greater than 0.3, which indicates that they are very likely mergers.

2.2. ALFALFA and Sample Matching

The main H I sample used in this paper is from the Arecibo Legacy Fast ALFA (ALFALFA) survey (Haynes et al. 2011, 2018). We use the 100% ALFALFA extragalactic H I source catalog, which contains 31,502 H I detections. Both "code I" and "code II" detections (see details in Haynes et al. 2011) are used in our work. The final H I sample contains 14,640 sources in the redshift range of 0.02–0.05 in the ALFALFA-SDSS overlap region (∼4000 deg^2).

The most probable optical counterpart (OC) of each H I detection has been assigned in the ALFALFA catalog. The ALFALFA H I detections and SDSS galaxies are then cross-matched using the following criteria: (1) the spatial separation between the OC and SDSS galaxy is less than 5″; (2) the velocity difference between the H I source and SDSS galaxy is less than 300 km s^{-1}. With these selection criteria, the matched sample consists of 10,972 galaxies in the redshift range of 0.02–0.05.

The measured H I spectra may be contaminated by close companions due to the large Arecibo beam (∼4′). Multiple SDSS galaxies within the beam radius and within a velocity difference of three times the H I line width (W_{50}) were excluded as potential H I contaminants. About 1300 galaxies were removed. Including these galaxies with ambiguous H I measurements produces negligible changes to the results presented in this paper. The final SDSS-ALFALFA matched sample used in our analysis contains 9595 galaxies.

Both the SDSS spectroscopy sample and the ALFALFA sample are from flux-limited surveys. Faint sources are progressively missed at higher redshifts. The SDSS spectroscopic selection $r < 17.77$ is roughly complete at $z = 0.05$ above a stellar mass of $\sim 10^{9.2}\ M_\odot$ for star-forming galaxies; for passive galaxies, the corresponding limit is $\sim 10^{9.8}\ M_\odot$. The ALFALFA sample is approximately complete at $z = 0.05$ above an H I gas mass of $\sim 10^{9.8}\ M_\odot$ for $W_{50} = 100\ \mathrm{km\ s^{-1}}$ and of $\sim 10^{10.2}\ M_\odot$ for $W_{50} = 400\ \mathrm{km\ s^{-1}}$. To include the population of galaxies with lower stellar masses and H I masses in our analysis, we corrected our sample by using the "$V_{\rm max}$ method." In detail, we calculated the maximum redshift at which the galaxy can still be detected according to the ALFALFA and SDSS sensitivity limit. The maximum redshift was then used to calculate the observable maximum comoving volume ($V_{\rm max}$) for each galaxy. By assuming the spatial distribution of our sample is homogenous in the comoving space, we weight each galaxy using the value of $V_{\rm total}/V_{\rm max}$ to account for the galaxies missed in the surveys, where $V_{\rm total}$ is the total comoving volume that our sample spans. The corrections of the SDSS and ALFALFA sample are performed independently and they are combined together to correct the matched sample.

2.3. GASS and COLD GASS

The data from a deeper H I survey, *Galaxy Evolution Explorer* Arecibo SDSS Survey (GASS; Catinella et al. 2013), is also used in this work. The representative GASS sample includes 47 central disk galaxies and 43 central elliptical galaxies in the stellar mass range of $10^{10.6}$–$10^{11}\ M_\odot$. A randomly selected subset of the GASS parent sample were observed in CO(1−0) in the COLD GASS survey using the IRAM 30 m telescope (Saintonge et al. 2011), which is used for the study of molecular gas in this work. The COLD GASS sample includes 28 central disk galaxies in the stellar mass range of $10^{10.6}$–$10^{11}\ M_\odot$.

For the massive galaxies concerned in this paper, a detection limit of $M_{\rm H\,I}/M_* \approx 0.015$ was reached in the GASS survey and $M_{\rm H_2}/M_* \approx 0.015$ was reached in the COLD GASS survey. To correct the flat $\log M_*$ distribution of these samples, each galaxy was weighted according to its stellar mass such that the weighted $\log M_*$ distribution is similar to that of all SDSS galaxies.

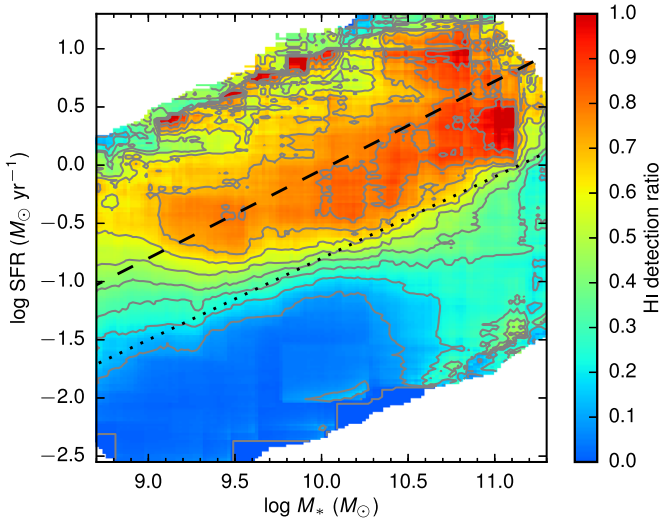

Figure 1. H I detection ratio in ALFALFA as a function of stellar mass (M_*) and star formation rate (SFR), determined within moving boxes of size 0.5 dex in mass and 0.5 dex in SFR. Each galaxy is weighted by a correction factor to account for selection effects. The dashed line indicates the position of the star-forming main sequence defined in Renzini & Peng (2015). The dotted line indicates the approximate divide between star-forming and quiescent galaxies according to their bimodal distribution in the SFR–M_* plane.

3. Results

3.1. Atomic Hydrogen Gas

With the $V_{\rm max}$ correction described in Section 2.2, we calculated the H I detection ratio for SDSS galaxies in the SDSS-ALFALFA overlap region in the redshift range of 0.02–0.05. The value of the corrected H I detection ratio in ALFALFA can be regarded as the fraction of galaxies with $M_{\rm H\,I} > 10^{9.3}\ M_\odot$, which is the ALFALFA detection limit at $z \sim 0.02$ for typical massive galaxies with H I line width of 300 km s^{-1}.

Figure 1 shows the H I detection ratio in the SFR–M_* plane for all SDSS galaxies. On average the H I detection ratio is above 70% for star-forming galaxies on the main sequence, and it drops rapidly toward the passive sequence (below the dotted line). The very low H I detection ratio (less than 10% on average) for quiescent galaxies suggests that the quenching process may significantly impact the H I gas content in galaxies. However, it is surprising that H I is also detected in about 30% of the massive quiescent galaxies with stellar mass above the Schechter characteristic mass $M_* \approx 10^{10.6}\ M_\odot$. What makes them different from the other 70% of massive quiescent galaxies with no H I detection? After a thorough examination of all observable parameters against these two populations of massive quiescent galaxies with and without H I detection, we find that almost all quiescent disk galaxies have H I detections, while quiescent ellipticals do not.

Since the extended H I gas is very sensitive to environmental effects (e.g., Giovanelli & Haynes 1985; Catinella et al. 2013), we only focus on central galaxies in the following analyses. We also selected a narrow stellar mass bin of $10^{10.6}$–$10^{11}\ M_\odot$ to minimize the effect of the dependence of SFR and gas mass on stellar mass. The left panel of Figure 2 shows the SFR distribution of central disk galaxies (blue line) and central elliptical galaxies (red line) in this stellar mass range and the gray line shows the fraction of disks relative to all galaxies (including 30% of the galaxies with uncertain morphology). It is well known that at a given stellar mass the distribution of SFR is bimodal (Kauffmann et al. 2003; Baldry et al. 2006). However, once we separate the galaxy population into disk galaxies and elliptical galaxies, the bimodality disappears. Although the quiescent galaxies are dominated by ellipticals, there is a substantial population of quenched disk galaxies.

The shaded regions in the left panel of Figure 2 show the SFR distribution of galaxies with H I detection. It is clear that almost all central disks have H I detection in ALFALFA from star-forming ones to the quiescents, while only a few central ellipticals have H I detection. The H I detection ratio of these galaxies is then quantified in the middle panel of Figure 2. From the star-forming main sequence to the passive sequence, the average H I detection ratio for central disk galaxies is ∼90% in ALFALFA and also in the deeper GASS survey, which implies that nearly all massive quiescent central disk galaxies have significant amounts of H I gas, e.g., with an H I gas fraction of $M_{\rm H\,I}/M_* > 0.1$.

The right panel of Figure 2 shows the average H I gas mass to stellar mass ratio ($M_{\rm H\,I}/M_*$) as a function of SFR for central disk galaxies. In ALFALFA, each galaxy has been weighted using the "$V_{\rm max}$ method" to correct the selection bias when deriving the average value. With this correction, our central disk galaxy sample has a very high H I detection ratio of ∼90%, hence the H I-detected central disk galaxies can be used as a fair representation of the whole sample of central disk galaxies. Encouragingly, the derived average value of $M_{\rm H\,I}/M_*$ from ALFALFA (dark blue line in the right panel of Figure 2) is very similar to the one derived from GASS (light blue line), which is a deeper representative sample (though with a much smaller sample size). Figure 2 clearly shows that, when SFR drops progressively from the star-forming main sequence to the passive sequence, the average H I gas mass of central disk galaxies remains almost the same. Massive quiescent central disk galaxies are surprisingly as abundant in H I gas as star-forming galaxies.

As shown by the red lines in Figure 2, the H I detection ratio for central ellipticals is only 10%–20%. In the GASS survey, the upper limits of $M_{\rm H\,I}/M_*$ for the nondetections are well constrained (down to 0.015). Thus, we calculate the average value of $M_{\rm H\,I}/M_*$ for central ellipticals by including the upper limits of nondetections in GASS, as shown by the pink arrows. The average H I gas mass in central ellipticals is much lower than that of quiescent central disk galaxies. The very low amount of H I gas in the overall quiescent population shown in previous literature is due to the increasing fraction of elliptical galaxies when SFR decreases.

The SDSS *gri* composite images of randomly selected examples of the star-forming disks, quiescent disks, and quiescent ellipticals are shown in Figure 3. We inspected all of the H I spectra for central disk galaxies in the stellar mass range of $10^{10.6}$–$10^{11}\ M_\odot$ in ALFALFA. Similar to star-forming ones, most quiescent central disk galaxies show characteristically symmetric double-horn H I profiles, indicating regularly rotating H I disks with little significant kinematic perturbations or contributions from companions, extra-planar gas, or tidal tails. As shown in the right panel of Figure 3, the stacked H I spectra for star-forming and quiescent disk galaxies show little difference.

3.2. Molecular Hydrogen Gas and Dust

The substantial H I gas amount in massive quiescent central disk galaxies indicates that these quenched galaxies have

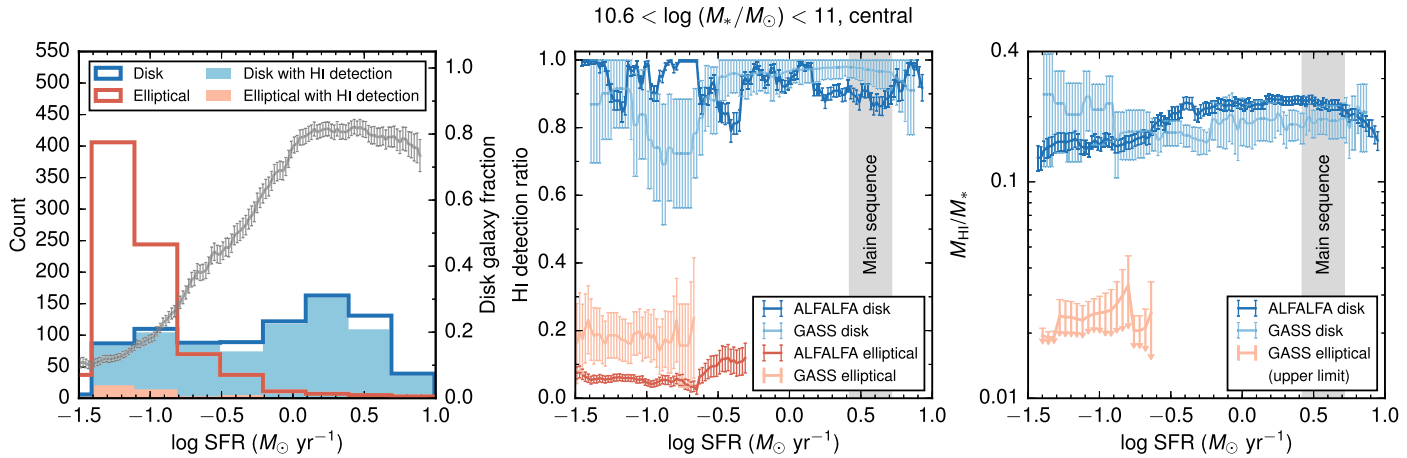

Figure 2. Left: SFR distribution function for central disk galaxies (blue line) and central elliptical galaxies (red line) in the narrow stellar mass range of $10^{10.6}$–10^{11} $M_\odot$. The shaded regions show the SFR distribution of galaxies with H I detection, in blue for central disks and in red for central ellipticals. About 30% of the galaxies with uncertain morphology are not shown here. The gray line shows the fractional abundance of disk galaxies, obtained by using a sliding average of 0.5 dex in SFR. Error bars are derived from the binomial error of the fraction with 68% confidence level. Middle: H I detection ratio in ALFALFA and GASS as a function of SFR for central disk galaxies (blue lines) and central elliptical galaxies (red lines) in the stellar mass range of $10^{10.6}$–10^{11} $M_\odot$. These values are determined by using the sliding average of 0.5 dex in SFR, and error bars are derived from the binomial error of the fraction with 68% confidence level. Right: H I gas mass to stellar mass ratio ($M_{\rm H\,I}/M_*$) for central disk galaxies and central elliptical galaxies (upper limit) in the same stellar mass range. For elliptical galaxies in GASS, the upper limits of nondetections are included in the average so that it is plotted as pink arrows. The error bars on the lines indicate the 1σ uncertainty around the mean value. The gray shades indicate the position of the star-forming main sequence defined in Renzini & Peng (2015).

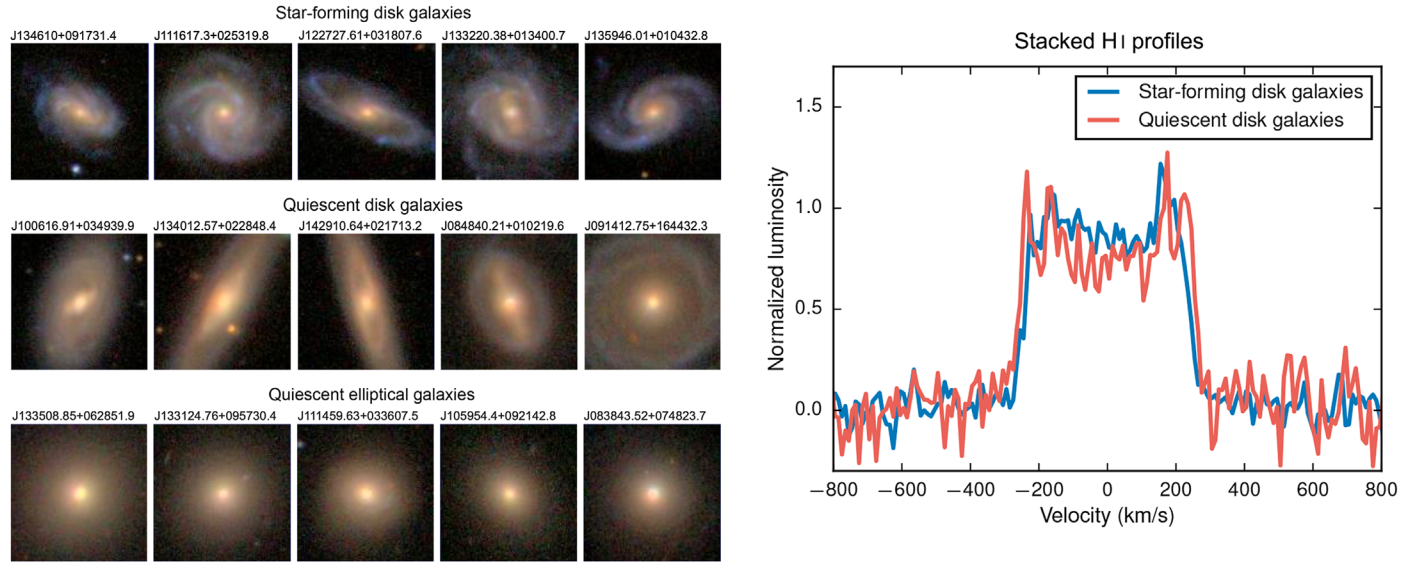

Figure 3. Left: SDSS *gri* composite images of randomly selected central galaxies in the stellar mass range of $10^{10.6}$–10^{11} $M_\odot$ for star-forming disk galaxies (top), quiescent disk galaxies (middle), and quiescent elliptical galaxies (bottom). The size of each image is 50 × 50 arcsec^2. Right: Stacked H I profiles for star-forming and quiescent central disk galaxies in ALFALFA. Galaxies with inclination angle $i > 60°$ (nearly edge-on) in the stellar mass range of $10^{10.6}$–10^{11} $M_\odot$ are selected for stacking. Before stacking, each spectrum is normalized by the integrated luminosity, and the velocity of each channel is divided by a factor of sin i to correct the projection effect. Star-forming and quiescent galaxies are divided by the dotted line in Figure 1.

enough raw material to fuel star formation. The low level of SFR of these galaxies hence requires that the H I gas cannot be effectively converted into H_2, and/or the H_2 gas has very low star formation efficiency ($\varepsilon_{H_2} = {\rm SFR}/M_{H_2}$). Although it is well known that quiescent galaxies have lower molecular gas mass and ε_{H_2} on average compared to star-forming ones (e.g., Saintonge et al. 2012; Tacconi et al. 2018), it remains unclear what would result if we only select central disk galaxies.

The left panel of Figure 4 shows the mean H I (in blue) and H_2 gas mass (in red) as a function of SFR for the central disk galaxies in the stellar mass range of $10^{10.6}$–10^{11} $M_\odot$ in the COLD GASS sample. The upper limits of the only galaxy without H I detection and the only galaxy without H_2 detection are shown as arrows and are not included to derive the average gas mass. As SFR decreases from the star-forming sequence to the passive sequence, the mean H I gas mass remains largely the same, while the mean H_2 gas mass decreases by a factor of ~10. The gray lines mark three different constant values of the star formation efficiency. As SFR drops, ε_{H_2} also drops by about a factor of 10, from 1 Gyr^{-1} to 0.1 Gyr^{-1}.

The dust content provides an alternative estimate of the gas mass in galaxies (e.g., Leroy et al. 2011). The Balmer decrement (Hα/Hβ) can be used as a proxy for dust content (Kennicutt 1992) inside the SDSS fiber of 3″, corresponding to

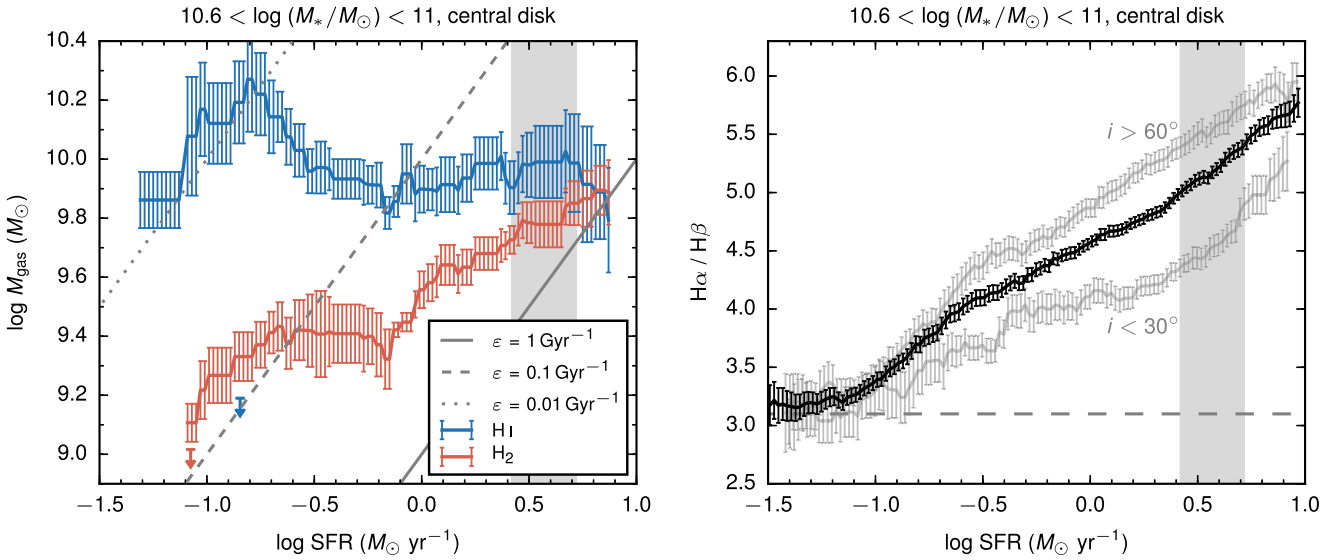

Figure 4. Left: the average atomic gas mass (in blue) and molecular gas mass (in red) as a function of SFR, from star-forming sequence to passive sequence, for central disk galaxies in the stellar mass range of $10^{10.6}$–10^{11} $M_\odot$ in COLD GASS. The narrow stellar mass bin is used to minimize the effect of dependence of SFR and gas mass on stellar mass. The blue arrow shows the H I mass upper limit of the only galaxy without H I detection and the red arrow shows the H_2 mass upper limit of the only galaxy without H_2 detection. These nondetections are not included to derive the average gas mass. The gray lines indicate the constant star formation efficiency for three different values. Right: the average value of Balmer decrement (Hα/Hβ) for all central disk galaxies (black line), for those with $i < 30°$ (nearly face-on, lower gray line), and for those with $i > 60°$ (nearly edge-on, upper gray line), within the same stellar mass range in SDSS. The horizontal dashed line indicates the intrinsic value of 3.1 without dust extinction. In each panel, the gray shading indicates the position of the star-forming main sequence. The average values are calculated in the sliding box of 0.5 dex in SFR; error bars on each line indicate the 1σ uncertainty around the mean value.

1.2–3 kpc in the redshift range of $z = 0.02$–0.05. The black line in the right panel of Figure 4 shows that the mean value of the Balmer decrement for these galaxies drops rapidly with decreasing SFR. Since the dust attenuation depends on the inclination angle i of galaxies, we also plot the mean values of Hα/Hβ for galaxies with $i < 30°$ (nearly face-on) and $i > 60°$ (nearly edge-on). The inclination angle indeed has an impact on the value of Hα/Hβ, but the trend remains unchanged.

Since the gas in the central region of galaxies is dominated by H_2 (Leroy et al. 2008), the decrease of dust attenuation with decreasing SFR provides independent support of the trend for H_2 shown in the left panel of Figure 4. It is interesting to note that the passive central disk galaxies with the lowest observable SFRs have Hα/Hβ close to the intrinsic value of 3.1 (horizontal dash line) for a hard radiation field (Osterbrock & Ferland 2006). Since these quiescent galaxies with emission lines are dominated by LI(N)ERs (Belfiore et al. 2017; Guo et al. 2019), the Hα/Hβ with an average value of ~3.1 indicates that there is little dust and gas in the central region of these quiescent disk galaxies.

As discussed in the Appendix, the main results presented in Figures 2 and 4 can be greatly affected by inaccurate SFRs due to aperture corrections and/or extinction corrections. Therefore, we repeat our analysis by using the SFRs derived from the SED fitting of UV, optical, and mid-IR bands (Salim et al. 2018). As shown in Figures 5 and 6 in the Appendix, all trends remain qualitatively the same as those in Figures 2 and 4.

4. Summary and Discussion

In order to investigate the detailed quenching process with an internal physical origin, we studied the cold gas content in massive central disk galaxies in the local universe. Our results show that massive quiescent central disk galaxies surprisingly have a similarly large amount of H I gas as star-forming ones. These galaxies are quenched because of their significantly reduced molecular gas and dust content and lower star formation efficiency.

The H I surface density in the outer regions of disk galaxies follows a homogenous radial profile when the radius is normalized by the diameter of the H I disk (Broeils & Rhee 1997; Wang et al. 2016). As mentioned above, quiescent central disk galaxies exhibit similarly symmetric characteristic double-horn H I profiles as star-forming systems, strongly suggesting that both galaxy types have regularly rotating H I disks. The almost constant H I gas mass of ~10^{10} $M_\odot$ (Figure 4), across the entire observable range of SFR, corresponds to H I disks with radii of ~30 kpc (Broeils & Rhee 1997; Wang et al. 2016). Thus, the H I gas in quenched disks may be stored in an outer ring such as in the prototypical case of the S0 galaxy NGC 1543 (Murugeshan et al. 2019).

This observational evidence suggests the following picture. Since the H I gas is distributed on very large scales (Leroy et al. 2008), once the central H_2 gas is consumed by star formation, expelled by outflows (Fabian 2012; Hopkins et al. 2014; Harrison 2017; Yuan et al. 2018), or ionized/photodissociated by UV radiation from AGNs (Fabian 2012), the timescale for the H I gas with high angular momentum in the outer disk to migrate inward may be very long in the absence of perturbations (Renzini et al. 2018). Therefore, during the quenching process, the rotationally supported outer H I disk remains largely unchanged. The SFR decreases, driven by the decreasing H_2 gas mass in the central region and progressively suppressed H_2 star formation efficiency (see Figure 4), with the gas remaining atomic rather than replenishing the star-forming molecular phase. The implications of these findings for the quenching of star formation in disk galaxies are further explored in Peng & Renzini (2019) and C. Zhang et al. (2019, in preparation).

We thank Robert Kennicutt, Sandra Faber, Nick Scoville, Barbara Catinella, Renbin Yan, and Jing Wang for useful discussions. We thank the ALFALFA team for providing the H I spectra of the ALFALFA extragalactic sample. Y.P. acknowledges National Key R&D Program of China Grant 2016YFA0400702 and NSFC grant No. 11773001. L.C.H. acknowledges National Key R&D Program of China Grant 2016YFA0400702 and NSFC grant No. 11473002 and 11721303. C.Z. acknowledges the NSFC grant No. 11373009 and 11433008. R.M. acknowledges ERC Advanced Grant 695671 "QUENCH" and support by the Science and Technology Facilities Council (STFC). A.D. acknowledges support from the grants NSF AST-1405962, GIF I-1341-303.7/2016, and DIP STE1869/2-1 GE625/17-1. Q.G. acknowledges NSFC grant Nos. 11573033 and 11622325, and the Newton Advanced Fellowships. F.M. acknowledges support from the INAF PRIN-SKA 2017 program 1.05.01.88.04. D.L. acknowledges NSFC grant Nos. 11690024 and 11725313. A.R. acknowledges support from an INAF/PRIN-SKA 2017 (ESKAPE-HI) grant.

Appendix
Alternative SFR Estimates

The main results presented in Figures 2 and 4 can be greatly affected by inaccurate SFRs, for instance due to inaccurate aperture corrections or extinction corrections. To address this concern, we repeat our analysis by using SFRs derived from the SED fitting of UV, optical, and mid-IR bands (GSWLC-M2 catalog; Salim et al. 2016, 2018). The results are shown in Figure 5 and the left panel of Figure 6. The SFRs used in the right panel of Figure 6 are given by the xCOLD GASS catalog

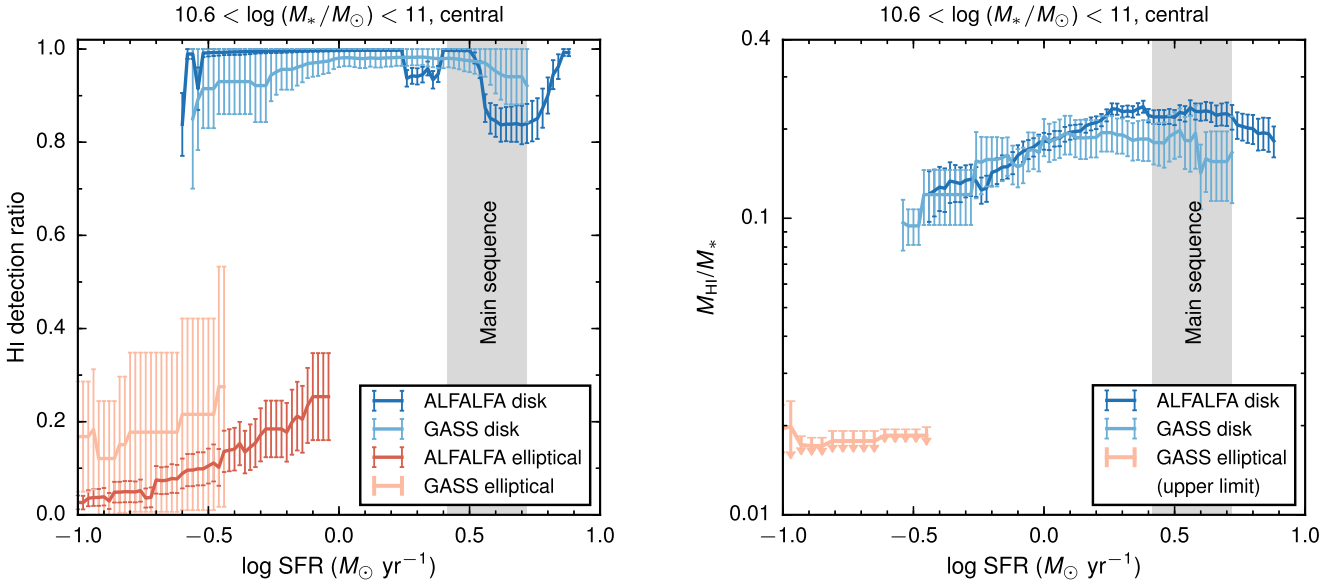

Figure 5. H I detection ratio and H I gas mass to stellar mass ratio ($M_{\rm H\,I}/M_*$) for central disk galaxies (blue lines) and central elliptical galaxies (red lines) in the stellar mass range of $10^{10.6}$–10^{11} $M_\odot$, plotted by using the SFRs derived from the SED fitting of UV, optical, and mid-IR bands (Salim et al. 2018). All labels in this plot are the same as those in Figure 2.

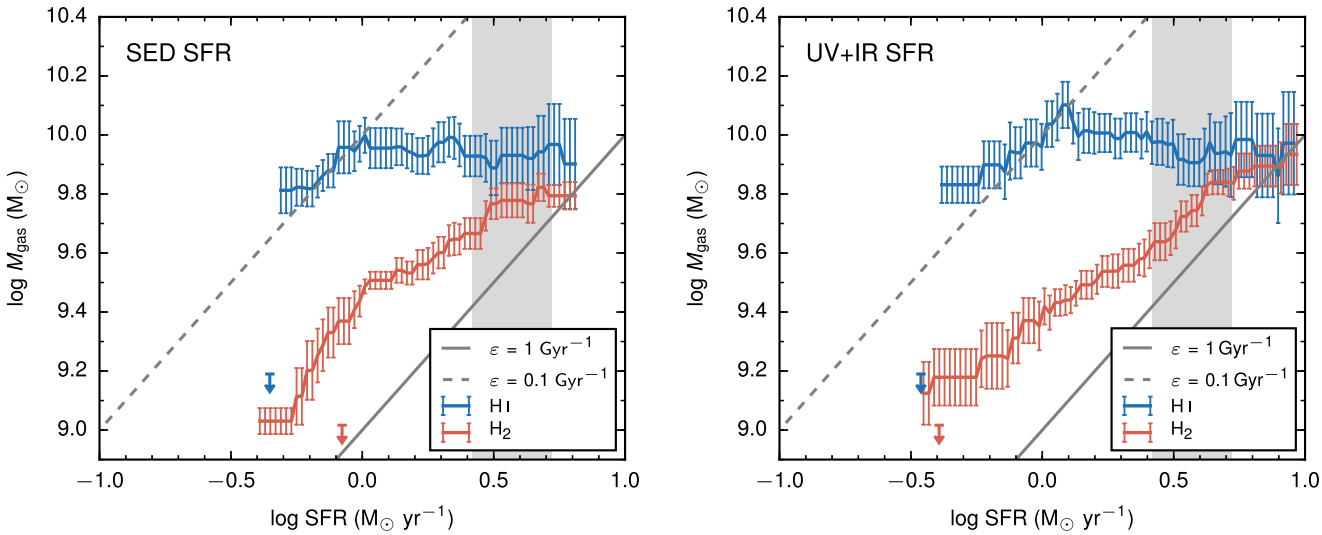

Figure 6. Average atomic gas mass (in blue) and molecular gas mass (in red) as a function of SFR for central disk galaxies in the stellar mass range of $10^{10.6}$–10^{11} $M_\odot$, plotted by using two different SFR estimates. The SFRs used in the left panel are derived from the SED fitting of UV, optical, and mid-IR bands (Salim et al. 2018). The SFRs used in the right panel are given by the xCOLD GASS catalog (Saintonge et al. 2017) and they are derived from the near-UV and mid-IR photometries by the technique described in Janowiecki et al. (2017). All labels in this plot are the same as those in Figure 4.

(Saintonge et al. 2017) and are derived from the near-UV and mid-IR photometries by the technique described in Janowiecki et al. (2017). For both of these two alternative SFR estimates, the dynamical range of SFRs for quiescent disk galaxies becomes smaller; however, the general trends of these plots remain the same. For disk galaxies with SFRs well below the main sequence (∼1 dex lower), the mean H I gas mass and H I detection ratio are still similar to those of star-forming galaxies as shown in Figure 5, while their H_2 gas mass decreases by a factor of ∼10 during quenching as shown in Figure 6. The drop of star formation efficiency (ε_{H_2}) becomes smaller compared to that of the MPA-JHU SFR.

ORCID iDs

Chengpeng Zhang https://orcid.org/0000-0001-6469-1582
Luis C. Ho https://orcid.org/0000-0001-6947-5846
Roberto Maiolino https://orcid.org/0000-0002-4985-3819
Avishai Dekel https://orcid.org/0000-0003-4174-0374
Filippo Mannucci https://orcid.org/0000-0002-4803-2381
Di Li https://orcid.org/0000-0003-3010-7661
Feng Yuan https://orcid.org/0000-0003-3564-6437
Alvio Renzini https://orcid.org/0000-0002-7093-7355
Kexin Guo https://orcid.org/0000-0001-6103-2821
Zhongyi Man https://orcid.org/0000-0001-9463-2444
Qiong Li https://orcid.org/0000-0002-3119-9003

References

Abazajian, K. N., Adelman-McCarthy, J. K., Agüeros, M. A., et al. 2009, ApJS, 182, 543
Baldry, I. K., Balogh, M. L., Bower, R. G., et al. 2006, MNRAS, 373, 469
Belfiore, F., Maiolino, R., Maraston, C., et al. 2017, MNRAS, 466, 2570
Blanton, M. R., & Roweis, S. 2007, AJ, 133, 734
Brinchmann, J., Charlot, S., White, S. D. M., et al. 2004, MNRAS, 351, 1151
Broeils, A. H., & Rhee, M.-H. 1997, A&A, 324, 877
Brown, T., Catinella, B., Cortese, L., et al. 2015, MNRAS, 452, 2479
Bruzual, G., & Charlot, S. 2003, MNRAS, 344, 1000
Catinella, B., Saintonge, A., Janowiecki, S., et al. 2018, MNRAS, 476, 875
Catinella, B., Schiminovich, D., Cortese, L., et al. 2013, MNRAS, 436, 34
Chabrier, G. 2003, PASP, 115, 763
Croton, D. J., Springel, V., White, S. D. M., et al. 2006, MNRAS, 365, 11
Dekel, A., & Birnboim, Y. 2006, MNRAS, 368, 2
Dekel, A., & Birnboim, Y. 2008, MNRAS, 383, 119
Emsellem, E., Cappellari, M., Krajnović, D., et al. 2011, MNRAS, 414, 888
Fabello, S., Catinella, B., Giovanelli, R., et al. 2011, MNRAS, 411, 993
Fabian, A. 2012, ARA&A, 50, 455
Genzel, R., Förster Schreiber, N. M., Lang, P., et al. 2014, ApJ, 785, 75
George, K., Subramanian, S., & Paul, K. T. 2019, A&A, 628, A24
Geréb, K., Catinella, B., Cortese, L., et al. 2016, MNRAS, 462, 382
Geréb, K., Janowiecki, S., Catinella, B., Cortese, L., & Kilborn, V. 2018, MNRAS, 476, 896
Giovanelli, R., & Haynes, M. P. 1985, ApJ, 292, 404
Guo, K., Peng, Y., Shao, L., et al. 2019, ApJ, 870, 19
Harrison, C. M. 2017, NatAs, 1, 165
Haynes, M. P., Giovanelli, R., Kent, B. R., et al. 2018, ApJ, 861, 49
Haynes, M. P., Giovanelli, R., Martin, A. M., et al. 2011, AJ, 142, 170
Hopkins, P. F., Hernquist, L., Cox, T. J., & Kereš, D. 2008, ApJS, 175, 356
Hopkins, P. F., Kereš, D., Oñorbe, J., et al. 2014, MNRAS, 445, 581
Huang, S., Haynes, M. P., Giovanelli, R., & Brinchmann, J. 2012, ApJ, 756, 113
Janowiecki, S., Catinella, B., Cortese, L., et al. 2017, MNRAS, 466, 4795
Kauffmann, G., Heckman, T. M., Simon White, D. M., et al. 2003, MNRAS, 341, 33
Kauffmann, G., White, S. D. M., Heckman, T. M., et al. 2004, MNRAS, 353, 713
Kennicutt, R. C., Jr. 1992, ApJ, 388, 310
Larson, R. B., Tinsley, B. M., & Caldwell, C. N. 1980, ApJ, 237, 692
Leroy, A. K., Bolatto, A., Gordon, K., et al. 2011, ApJ, 737, 12
Leroy, A. K., Walter, F., Brinks, E., et al. 2008, AJ, 136, 2782
Lintott, C., Schawinski, K., Bamford, S., et al. 2011, MNRAS, 410, 166
Martig, M., Bournaud, F., Teyssier, R., & Dekel, A. 2009, ApJ, 707, 250
Masters, K. L., Mosleh, M., Romer, A. K., et al. 2010, MNRAS, 405, 783
Mihos, J. C., & Hernquist, L. 1996, ApJ, 464, 641
Murugeshan, C., Kilborn, V., Obreschkow, D., et al. 2019, MNRAS, 483, 2398
Osterbrock, D. E., & Ferland, G. J. 2006, Astrophysics of Gaseous Nebulaeand Active Galactic Nuclei (2nd ed.; Mill Valley, CA: Univ. Science Books)
Parkash, V., Brown, M. J. I., Jarrett, T. H., Fraser-McKelvie, A., & Cluver, M. E. 2019, MNRAS, 485, 3169
Peng, Y., Maiolino, R., & Cochrane, R. 2015, Natur, 521, 192
Peng, Y.-j., Lilly, S. J., Kovač, K., et al. 2010, ApJ, 721, 193
Peng, Y.-j., Lilly, S. J., Renzini, A., & Carollo, M. 2012, ApJ, 757, 4
Peng, Y.-j., & Renzini, A. 2019, MNRAS, submitted
Renzini, A., Gennaro, M., Zoccali, M., et al. 2018, ApJ, 863, 16
Renzini, A., & Peng, Y.-j. 2015, ApJL, 801, L29
Saintonge, A., Catinella, B., Cortese, L., et al. 2016, MNRAS, 462, 1749
Saintonge, A., Catinella, B., Tacconi, L. J., et al. 2017, ApJS, 233, 22
Saintonge, A., Kauffmann, G., Kramer, C., et al. 2011, MNRAS, 415, 32
Saintonge, A., Tacconi, L. J., Fabello, S., et al. 2012, ApJ, 758, 73
Salim, S., Boquien, M., & Lee, J. C. 2018, ApJ, 859, 11
Salim, S., Lee, J. C., Janowiecki, S., et al. 2016, ApJS, 227, 1
Salim, S., Rich, R. M., Charlot, S., et al. 2007, ApJS, 173, 267
Schommer, R. A., & Bothun, G. D. 1983, AJ, 88, 577
Tacconi, L. J., Genzel, R., Saintonge, A., et al. 2018, ApJ, 853, 179
Tojeiro, R., Masters, K. L., Richards, J., et al. 2013, MNRAS, 432, 359
Wang, J., Koribalski, B. S., Serra, P., et al. 2016, MNRAS, 460, 2143
Yang, X., Mo, H. J., van den Bosch, F. C., et al. 2007, ApJ, 671, 153
Yang, X., Mo, H. J., van den Bosch, F. C., & Jing, Y. P. 2005, MNRAS, 356, 1293
Yuan, F., Yoon, D., Li, Y.-P., et al. 2018, ApJ, 857, 121